Band Engineering by Controlling vdW Epitaxy Growth Mode in 2D Gallium Chalcogenides

*Hui Cai, Emmanuel Soignard, Can Ataca, Bin Chen, Changhyun Ko, Toshihiro Aoki, Anupum Pant, Xiuqing Meng, Shengxue Yang, Jeffrey Grossman, Frank D.Ogletree, and Sefaattin Tongay**

Post transition metal chalcogenides (PTMCs), with the standard chemical formula MX (M = In, Ga, Sn, and X = S, Se, Te), have emerged as novel 2D semiconducting materials and shown their potentials in next generation optoelectronic applications.[1] As a member of PTMCs, GaSe is a layer structured material where two Ga atoms are sandwiched between two Se atoms to form the "X–M–M–X" structure. In contrast to group VI transition metal dichalcogenides, i.e., MoS_2 and WSe_2, GaSe has a direct gap in the bulk and few-layer form, but undergoes direct to indirect transition for flakes thinner than 5-layers.[2] Owing to the direct gap nature of few-layers and much reduced exciton binding energy related to weaker confinement effects, they are potential candidates for solar cells,[3] field effect transistors (FETs),[4] and photodetection applications[5–7] where excitons must be formed and separated efficiently. More recently, few-layered PTMCs have been shown to have nearly ideal band alignment with respect to redox reduction and oxidization potentials of water splitting, and thus proposed as potential material systems for H_2 generation and photo-electro-chemical cell applications.[8]

The van der Waals (vdW) epitaxy concept was first introduced by Koma nearly three decades ago when he demonstrated the synthesis of ultra-thin $NbSe_2$ few- and mono-layers on MoS_2.[9] Since then a large number of 2D-like materials have been synthesized onto surface passivated and active surfaces using molecular beam epitaxy systems without any constraint over lattice match conditions. Examples include $MoSe_2$,[10] WSe_2,[11] SnS_2,[12] $SnSe_2$,[12] $MoTe_2$,[13] InSe,[14] and even GaSe[3,6,7]—a focus of this article—onto mica, graphite, MoS_2, Si(111), and GaAs (111) surfaces with 5%–20% mismatch. Here, one important aspect of vdW epitaxy is that the grown layers are weakly coupled to the underlying substrates via vdW forces, independent from surface chemistry of the substrate, due to chemical inertness of 2D layers. Consequently, synthesized materials are expected to possess material properties close to their unperturbed (exfoliated) state, in agreement with recent reports on vdW epitaxy of WS_2, MoS_2, WSe_2, and 2D alloys on sapphire or SiO_2 substrates.[6,15] In contrast to common sense, our results demonstrate that material properties of GaSe deposited on Si(111) show stark differences compared to vdW epitaxy on sapphire as well as pristine exfoliated samples.

Herein, we for the first time demonstrate that vdW epitaxy can be utilized to create materials with properties vastly different from their most relaxed state. Our studies show that vdW epitaxy of GaSe on Si(111) reduces the band gap of ultra-thin GaSe layers from their most commonly accepted value at 2 eV (620 nm) down to 1.7 eV (700 nm), resulting in colossal band renormalization. The band gap range is similar to that of $GaSe_xTe_{(1-x)}$ ternary alloys (1.65–2 eV for $x = 0$ to 1).[16] Results show that this effect is observed when layers are grown onto chemically active Si(111) surfaces, but not on passive sapphire, suggesting that the interaction between substrate and 2D material dictate the behavior of materials. Photoluminescence (PL), Raman spectroscopy, and high pressure diamond-anvil cell (DAC) studies reveal that despite chemically passivated GaSe surface and weak interlayer vdW coupling, underlying substrate manages to induce finite in-plane strain and significantly renormalize the optical band gap of GaSe. In traditional epitaxy, substrate induced strain has been widely used to tune the band gap and optical properties of the epitaxial film.[17] However, such method has not been reported in the vdW epitaxy of 2D materials.

Through the manipulation of kinetic factors of the physical vapor transport (PVT) process, such as synthesis temperature, cooling rates and amount of precursor, we were able to tune

H. Cai, B. Chen, A. Pant, Prof. X. Meng, Prof. S. Tongay
School for Engineering of Matter
Transport and Energy
Arizona State University
Tempe, AZ 85287, USA
E-mail: sefaattin.tongay@asu.edu
Prof. E. Soignard, Dr. T. Aoki
LeRoy Eyring Center for Solid State Science
Arizona State University
Tempe, AZ 85287, USA
Dr. C. Ataca, Prof. J. Grossman
Department of Materials Science and Engineering
Massachusetts Institute of Technology
Cambridge, MA 02139, USA
Dr. C. Ko
Department of Materials Science and Engineering
University of California
Berkeley, CA 94720, USA
Prof. S. Yang
School of Materials Science and Engineering
Beihang University
Beijing 100191, P. R. China
Dr. F. D. Ogletree
Materials Sciences Division
Lawrence Berkeley National Laboratory
Berkeley, California 94720, USA
Dr. F. D. Ogletree
Molecular Foundry
Lawrence Berkeley National Laboratory
Berkeley, CA 94720, USA

DOI: 10.1002/adma.201601184

ADVANCED MATERIALS
www.advmat.de

Materials Views
www.MaterialsViews.com

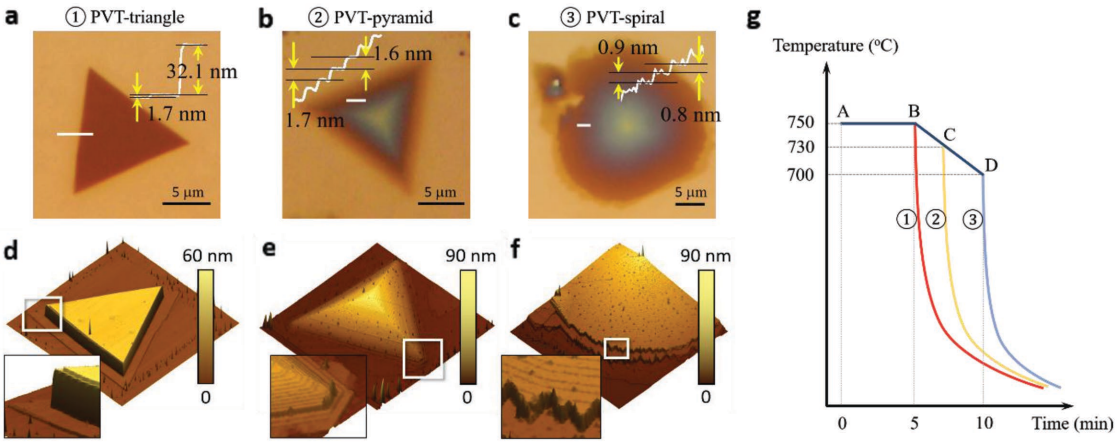

Figure 1. a) Optical images of GaSe triangle, b) pyramid, and c) spiral flake with AFM height profiles (inset). d) 3D height profiles of GaSe triangle, e) pyramid, and f) spiral flake with zoom-in view of the edges (inset). g) Temperature profile of the three growth processes.

the supersaturation concentration to stabilize screw-dislocation driven (SDD) and layer-by-layer (LBL)—also called Frank van der Merwe—growth modes. Resulting GaSe structures have striking pyramid, triangle, and spiral shapes where each interact with the substrate differently, and thus have different optical response. Overall, results are fundamentally and technologically intriguing as the technique offers unique routes to design materials without alloying or defect engineering, and sheds light on vdW epitaxy of low-dimensional systems.

Typical vdW of GaSe on Si(111) surface by PVT technique results in three different morphologies, namely flat triangle, spiral, and pyramid shapes as shown in **Figure 1**. Based on spectroscopy and pressure studies, each one of these possesses different material behavior. Since observed differences in their morphologies are essential to the understanding of why GaSe properties differ significantly from exfoliated or PVT on sapphire ones, we will first focus on growth mechanism and in the remainder of the article focus on vast differences across GaSe 2D crystals.

In a typical PVT, Ga_2Se_3, and GaSe precursors were transported to hot (growth) zone using inert Ar gas at high temperatures (see Experimental Section) to deposit GaSe layers on Si(111) and sapphire surfaces. Here, Si(111) surface offers an excellent hexagonal symmetry match between the matching faces of GaSe(0001) and Si(111) that corresponds to a 2.6% room temperature mismatch using a GaSe "*a*" lattice parameter of 3.74 Å and a silicon surface net parameter, $a/\sqrt{2} \approx 3.84$ Å.[18] In Figure 1a and d, we show optical and AFM images taken from triangular GaSe nanostructures which measures 30 nm in height with rather steep edges. A closer look at the AFM images shows that the triangle is grown on a bilayer GaSe plane measuring 1.7 nm in thickness—twice that of *c*-axis lattice parameter (Figure 1d and Figure S1, Supporting Information). In contrast, pyramid flake (Figure 1b,e) does not have sharp edges, but instead its edges make acute angle. Each step of pyramid structure is ≈1.6–1.7 nm in thickness which implies that GaSe layers are grown as bilayers (Figure 1b inset) in Bernal (AB) stacking. Unlike others, spiral flakes (Figure 1c,f) is made of monolayer GaSe which 0.9 nm step height, and can be clearly distinguished by its striking helical fringes and spiral contours. The chemical composition measured by energy dispersive X-ray spectroscopy (EDS) shows the Ga:Se ratio is close to 1:1 and the elemental mapping shows both Ga and Se distribute uniformly across the flake (Figure S4, Supporting Information). The chemical composition and its uniformity are further confirmed by nano-Auger technique whose lateral resolution is in the order of 10 nm (Figures S5 and S6, Supporting Information). Based on in-depth nano-AES results (Figure S6, Supporting Information), only a negligible amount of O atoms was detected at the GaSe/Si interface and the O/Si compositional ratio is estimated to be ≈0.02. This value is much lower than those of silicon oxides (O/Si ≈ 2) representing that the oxidation of Si was suppressed well during the growth. We mention that it is possible to observe GaSe formation on partially oxidized Si surface as GaSe growth is also allowed on SiO_2. TEM measurements show that synthesized flakes are in ε-phase where layers are stacked in Bernal stacking arrangement (Figure S7, Supporting Information). In such ABAB stacking, each unit cell contains two monolayers in the *c*-axis. In LBL growth, each "layer" is one unit cell where two monolayers are bonded together, leading to the bilayer stacking in pyramids. Whereas in SDD growth, the growth is triggered by the screw dislocation edge with the height of the burgers vector which is one monolayer, leading to the monolayer stacking in spiral flakes.

After careful optimization of growth conditions, we were able to develop a technique to favor (stabilize) the synthesis of particular feature over others through different cooling temperature profiles as shown in Figure 1g. In our growth process, samples were kept at growth temperature 750 °C for 5 min (see A→B in Figure 1g), and immediately after samples were cooled down to room temperature following three different paths (red, yellow, and blue lines). The first path (red curve in Figure 1g) predominantly produces flat triangles after rapidly cooling the furnace at a rate greater than 20 °C by simply opening tube furnace. For the second path (yellow curve), samples were cooled at a rate of 10 °C min^{-1} (B→C) within 2 min, and fast cooled (rate>20 °C) below 730 °C. Interestingly, pyramids are only formed during this process. For the third path (blue curve), samples are cooled down to 700 °C at a controlled rate of 10 °C min^{-1} and fast cooled down to room temperature

DOI: 10.1002/adma.201601184

below 700 °C. Flakes with spiral patterns are mostly observed after this process.

What is the origin of such vastly different morphologies and relation to growth conditions? The synthesis of crystalline nanomaterials must follow basic crystal growth theory, describing the LBL (also called Frank van der Merwe) dendritic growth,[19] and spiral SDD growth.[20] In this work, triangle and pyramid features are in the LBL regime due to their highly layered/stacked nature, whereas spiral flakes are grown by SDD (Figure S2, Supporting Information). The latter is particularly evident from spiral patterns in AFM images (Figure 1c and Figure S1, Supporting Information) which is a signature morphology observed in SDD grown low-dimensional materials. Within the crystal theory, dendritic LBL–SDD growth regime depends on the degree of supersaturation which is expressed as $\sigma = \ln(c/c_0)$ where c and c_0 are the precursor and equilibrium concentration values.[21] We postulate that triangle features are grown at 750 °C (A→B) when the precursor concentration is higher—due to higher vapor pressure—and σ value is high enough to sustain LBL growth. Upon rapid cooling, growth temperature quickly drops below 700 °C (above which GaSe layers are grown), bypassing B→C and C→D temperature regions, and thus almost no growth takes place below 750 °C. However, when the temperature is slowly cooled from 750 to 730 °C (B→C), precursor concentration, σ, and step growth velocity (v_i) slowly decreases (Figure S2, Supporting Information). Combination of these factors is still sufficient to sustain LBL growth (as evidenced by layered nature of pyramids), but resulting materials assume pyramid shapes due to reduced and time/temperature dependent v_i. Finally, spiral features are realized at low temperature (C→D), low precursor, and σ conditions. In this regime, nuclei formation—which is essential to LBL growth—is not preferred as the supersaturation concentration is below its critical value, instead screw dislocations offer active sites with relatively large Gibbs free energies and SDD growth dominates in the C→D range (see spiral image in Figure 1f). Since each layer measures monolayer (0.9 nm) in spiral features, as opposed to bilayers in triangles and pyramids, we argue that screw dislocations are probably formed by uplifted layers as shown in Figure S2 in the Supporting Information.

Colossal band renormalization in GaSe on Si(111). **Figure 2**b shows representative PL spectra taken from exfoliated GaSe (Figure 2a) and different locations across a triangle flat GaSe flake (Figure 2a). PL spectrum of triangle GaSe is significantly red-shifted compared to exfoliated ones, and similar studies on a large number GaSe flakes with spiral, triangular, and pyramid morphologies reveal vdW epitaxy on Si(111) overall produces red-shifted emission lines (Figure 2c). Depending on the morphology of GaSe flakes, their emission range covers from 620 to 700 nm which corresponds to almost the same spectral range attained by alloying Se with Te in $GaSe_xTe_{(1-x)}$ ternary systems[16] as shown in Figure 2d. Considering such broad range of band gap variation, we refer to this effect as "colossal band gap renormalization" for the rest of the article.

Interestingly, PL peak position of triangle and pyramid GaSe flakes ranges in the 620–700 and 640–700 nm respectively, whereas PL spectrum of spiral GaSe appears in close proximity to 680 nm with narrow PL distribution (σ_{PL} +/− 10 nm) as shown in Figure 2c. We note that PL peak position of exfoliated GaSe and vdW GaSe on sapphire both have very small variation, $\sigma_{PL} < 4$ nm, but emission lines are located at 620 and 630 nm which matches to the theoretically predicted and experimentally established values of GaSe. These trends can be clearly observed from PL peak position and intensity mapping data collected from various GaSe flakes in **Figure 3**. For example, spiral and exfoliated GaSe flakes possess relatively uniform PL intensity whereas emission intensity is largely non-uniform on

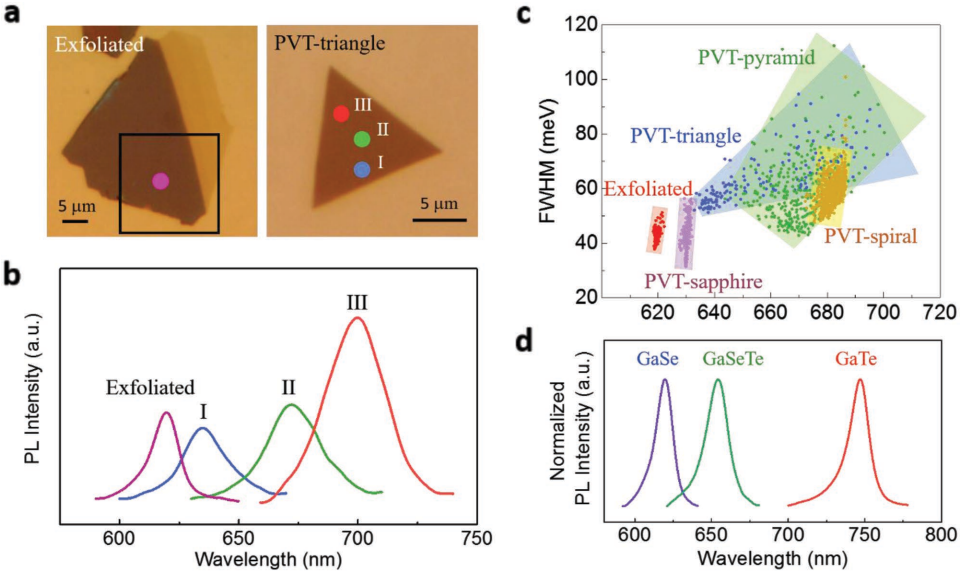

Figure 2. a) Optical images of an exfoliated GaSe flake and PVT synthesized GaSe triangle. b) PL spectra of the exfoliated flake and the PVT synthesized triangle, taken at locations pointed in a by dots with corresponding colors. c) Distribution of PL FWHM as a function of peak position for each case. The quadrilaterals are for eye-guidance. d) PL spectra of GaSe, GaSeTe alloy and GaTe.

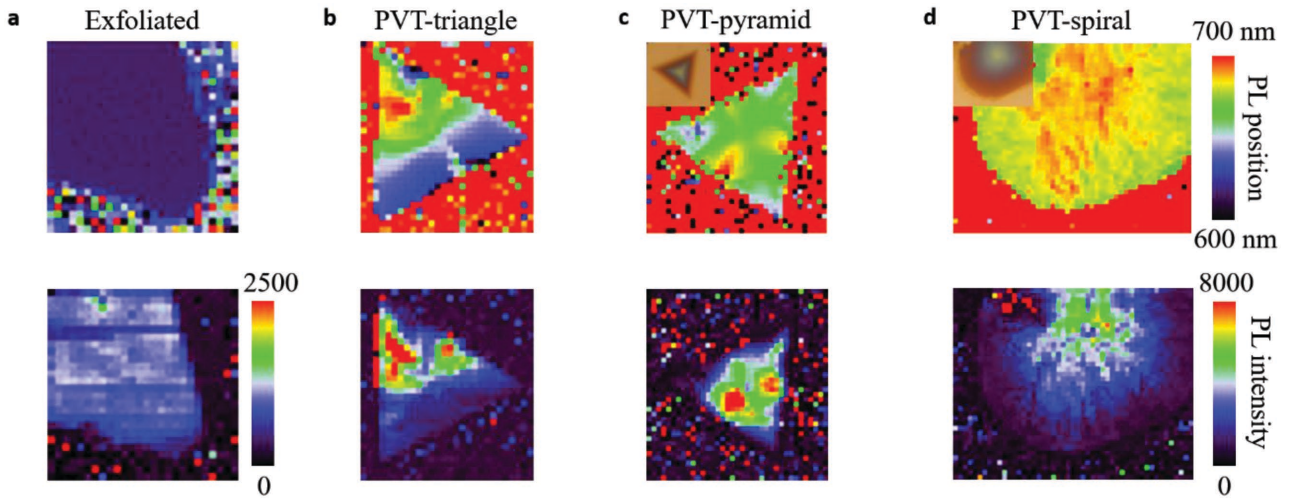

Figure 3. a) PL peak position and PL intensity mapping of exfoliated, b) PVT grown triangle, c) PVT grown pyramid, and d) PVT grown spiral GaSe flakes.

triangles and pyramids. Furthermore, PL intensity from vdW GaSe appears more luminescent compared to exfoliated ones.

The question arises: What is the origin of such large band gap change? Our results cannot be explained by the simple band renormalization due to quantum confinement effects in 2D systems with reduced thickness, since thickness can only significantly influence PL and Raman spectra in few-layered form (<5 nm).[22] In order to rule out the thickness effect on the band gap renormalization, we performed thickness dependent PL and Raman measurements on exfoliated GaSe on Si (Figure S3, Supporting Information). It clearly demonstrates that the PL remains at 2 eV for flakes thicker than 10 nm, and the intensity gradually decreases as thickness reduces. The Raman peaks are at fixed positions for all thickness, and gradually disappear as thickness decreases. In the PVT synthesized samples, the PL and Raman variation is observed at a thickness of 34 nm for the triangle, 10–70 nm for the pyramid, and 10–100 nm for the spiral flake (no PL or Raman can be measured when thickness is less than 10 nm due to low absorption). It is also noteworthy to point out that the PL and Raman variation is observed on a flat triangle (Figure 2a), where the thickness is all the same across the flake, but the PL is shifted by ≈80 nm and the intensity is changed by 100% (Figure 2b). This further confirms that the red shift of PL and Raman is not related to a thickness effect.

Another potential explanation might be non-stoichiometric elemental distribution across GaSe flake resulting in bound excitons ($X_D \rightarrow D$ + eh) trapped at various chalcogen vacancy sites with different light emission energy. However, nano-scale EDS reveals that 1:1 Ga/Se ratio is perfectly retained on the flake (Figure S4, Supporting Information). Lastly, band alignment across Si and GaSe is also not possible to yield red-shifted PL since these results are specific to vdW epitaxy on Si, and exfoliation onto Si(111) does not yield similar response. Colossal PL change, however, can be attributed to substrate induced strain effects on GaSe nanostructures as evidenced by micro-Raman spectroscopy measurements and DFT calculations.[23,24]

We argue that band renormalization effect originates from finite tensile strain acting on vdW deposited GaSe/Si(111) flakes. Micro-Raman studies on triangular GaSe flakes show that three prominent vibrational modes ($A_{1g}{}^1$, E_{2g}, and $A_{1g}{}^2$ located near 135, 214, and 307 cm^{-1}, respectively) are significantly softened compared to exfoliated GaSe (**Figure 4**a,b). Here, we note that triangular flakes offer ideal platform to perform Raman characterization owing to their uniform thickness and flat morphology. Even though presented results are acquired from triangles, similar findings have also been reproduced for a large number of spiral and pyramid GaSe samples. Red-shifted Raman peaks clearly implies that a finite tensile strain exists on GaSe/Si(111) compared to unstrained exfoliated GaSe.[24]

Further evidence for finite in-plane strain comes from lifted degeneracy of E_{2g} mode.[24,25] This mode, described by a single Lorentzian peak on exfoliated GaSe flakes, splits into two components, namely $E_{2g}{}^-$ and $E_{2g}{}^+$, for vdW GaSe/Si(111) (Figure 4a). In its unstained state the E_{2g} mode consists of two degenerate modes: one polarized in the *a*-axis and another in the *b*-axis direction as depicted in Figure 4c. But with finite strain at any arbitrary angle (ϕ), the degeneracy of $E_{2g}{}^-$ and $E_{2g}{}^+$ peaks is lifted, and each peak shifts by a different amount depending on the direction of the strain axis with respect to *a* and *b* lattice vectors. This picture is further supported by similar findings on strain/E_{2g} mode splitting relations observed on other material systems, such as CNTs, graphene, and more recently MoS_2.[24,25]

Importantly, Raman peaks gradually red-shift going from point I to III (see flake and labeling in Figure 2a), suggesting that the magnitude of the strain is not uniform across the flake. PL mapping on the same flake reveal that peak position is red-shifted and PL intensity much increased in the same direction (I to III). Thus, we argue that PL peak shift and band gap change is directly linked to the amount of strain within each flake, and PL mapping gives reasonable information on nanoscale strain distribution on the flake. Here, we note that strained parts have stronger emission possibly due to exciton immigration/diffusion from unstrained (larger band gap) regions to strained parts through funneling effect (see Figure 4e).[26] Proposed in-plane tensile strain picture is also consistent with the first principles

Adv. Mater. **2016**,
DOI: 10.1002/adma.201601184

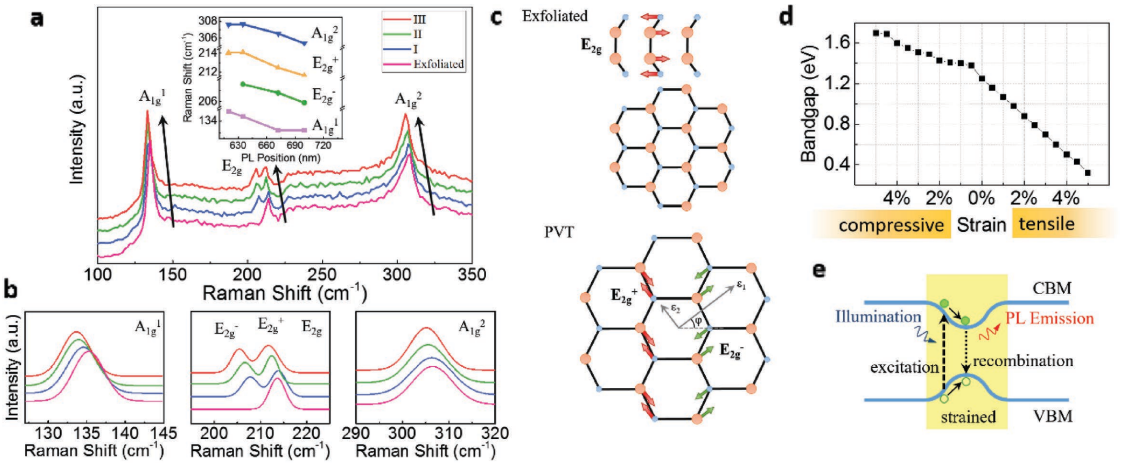

Figure 4. a) Raman spectra of the PVT synthesized GaSe triangle taken at locations indicated by the dots in Figure 2a with corresponding colors. The result is compared to an exfoliated (unstrained) GaSe flake on the same substrate. Inset: The shift of each vibration mode as a function of PL peak position as shown in Figure 2b. b), Fitted spectra of the vibration modes of A_{1g}^1, E_{2g}, and A_{1g}^2 on exfoliated and PVT synthesized triangle. c), Comparison of the vibration properties of unstrained GaSe and biaxial strained GaSe. d), DFT calculated bandgap as a function of strain. e), Schematic diagram of the funnel effect caused by non-uniform strain.

results (Figure 4d) which shows that band gap decreases (by 0.18 eV/%) in the tensile strain direction, whereas compressive strain increases the band gap by 0.11 eV/%. From the $dE_{gap}/d\sigma$ relation in Figure 4d, together with largest measured PL peak shift (2.0 eV for exfoliated GaSe to 1.7 eV for GaSe triangles), the maximum value of the in-plane tensile strain is estimated to be 2% which is the room temperature mismatch (2.6%) between Si(111) and GaSe.

Due to a larger lattice mismatch between GaSe and sapphire (21%), vdW epitaxy on sapphire produces GaSe flakes with physical properties close to exfoliated ones (see Figure 2c and Figure S8, Supporting Information). The PL peak is shifted only by 10 nm, which may be caused by minimal amount of strain induced by sapphire. Consequently, vdW epitaxy on sapphire produces flakes with narrow PL distribution (similar to exfoliated ones) whereas GaSe triangles and pyramids on Si span much larger energy range due to non-uniform strain distribution. The only exception to this trend is observed on spiral GaSe flakes on Si(111) where its PL peak position is significantly red-shifted and is well defined. It should be pointed out that even though the thickness of all these flakes is different, the variation in the PL peak position (PL mapping) is not simply a thickness effect. This is because i) quantum confinement effects, which leads to PL peak position and band renormalization for different thicknesses of GaSe, is not effective unless the thickness is less than 5 nm. However, in this work, studied effects originate from GaSe flakes that are thicker than 10 nm (see Figure S3 in the Supporting Information). ii) Moreover, the thickness and PL peak position do not match or show correlation with each other. More specifically, comparison between the triangle with the exfoliated flakes shows that even though they both have a flat surface and uniform thickness distribution, the PL peak position mapping appears quite differently. The exfoliated flake is quite uniform in both PL peak position and intensity, but the triangle shows a clear spatial variation. Similarly, for the pyramid case, the thickness gradually increases from the edge to the center by stacking smaller and smaller triangles on top. The pattern of thickness change can be seen in the optical and AFM images shown in Figure 1b,e. However, the PL mapping shows a quite different pattern as shown in Figure 3c, indicating weak correlation between thickness and PL. The PL mapping shows that the strain is localized at the center of the edge and relieved at the corners. This may be related to the self-induced local strain caused by interlayer stacking.[27] For the spiral case, PL intensity mapping and thickness correlates with each other, whereas PL peak position does not. Since the SDD growth is driven by misplaced edges and kinks due to lower activation energies, uniform PL peak distribution can be attributed to uniform strain profile on spiral flakes.

To understand the origin of strain in the synthesized GaSe flakes, we have performed further DFT studies and the details are given in the support information (Figure S9, Supporting Information). The inhomogeneity of the strain distribution is quite interesting, and can be explained in several ways. The presence of a finite strain on GaSe layers could be related to small lattice mismatch between Si and GaSe. When coupled with high surface reactivity of Si(111), interaction between GaSe and Si(111) influences the vdW epitaxy in such a way that it lowers the total energy of the system by introducing strain to synthesized layers. Since PL and Raman measurements probe the whole thickness of the GaSe, it is possible that thickness dependent strain is an integral effect where each layer contributes to overall PL and Raman response and variation (hence the large FWHM in PL). Observed inhomogeneity and strain could also be related to 1) presence of defects and dislocations on Si wafer. These defects may provide nucleation sites for the GaSe growth, where GaSe–Si interaction is strongest. As the flake grows out, the GaSe–Si interaction weakens and releases the strain. Alternatively, 2) another explanation could be the thermal expansion coefficient difference between Si (2.6 μm °C^{-1}) and GaSe (8.9 μm °C^{-1}). During the cooling process, the GaSe crystal shrinks faster than Si due to the much larger thermal expansion coefficient, and strong interaction between Si(111) and GaSe could lead to inhomogeneous strain.

Overall results are surprising since i) GaSe layers are perfectly passivated thus interaction with the underlying substrate is expected to be minuscule regardless from the substrate's chemical state, ii) even if there is a finite strain acting on GaSe layers, it is unlikely to transfer strain from one layer to another through weak vdW forces between adjacent layers. In this view, strain is anticipated to act only on the first few layers and PL/Raman measurements (which collects signal with equal weighting factor across the thickness) should—in principle—probe mostly unstrained regions. Considering results on Si(111), sapphire, and exfoliated flakes, underlying substrate plays an essential role in determining the material behavior of GaSe, especially when the substrate surface is not passivated as in the case of Si(111). One potential explanation is that Si atoms interact strongly with nucleated GaSe, and strain is carried onto GaSe layers during lateral diffusion process due to finite—but small—lattice mismatch. Strain is transferred to adjacent GaSe layers, perhaps due to energetic considerations, i.e., total energy of the system is minimized when successive layers are strained and Bernal stacked onto strained underlying layers.

Effect of the vertical compressive strain: Further evidence for in-plane strain comes from DAC measurements (see Experimental Section). In contrast to conventional DAC setup where hydrostatic pressure acts both in- and out-of-plane directions, we have applied compressive vertical pressure up to ≈0.3 GPa on GaSe nanostructures and monitored the shift in Raman frequencies and PL peak position. The pressure is estimated from the Si Raman peak shift (Figure S11, Supporting Information). If GaSe on Si(111) has a finite amount of tensile strain, we anticipate that GaSe layers will be easier pushed closer to each other at a given pressure due to increased bond length reducing the change density around individual GaSe layers and repulsion force between adjacent layers. Since the band gap and PL peak position strictly depends on the interlayer coupling, PL peak position of GaSe/Si(111) is expected to have stronger pressure dependence compared to exfoliated ones.

The pressure response of both PVT-grown triangle and spiral flakes are compared to the exfoliated GaSe flake as shown in **Figure 5** and Figure S10 in the Supporting Information. Upon applying pressure on spiral GaSe/Si(111) in DAC setup, Raman peaks gradually stiffen as shown in Figure 5b,c, suggesting that the applied pressure is successfully transferred to GaSe. PL spectroscopy and m-DAC measurements reveal that PL peak red-shifts for both GaSe/Si(111) and exfoliated GaSe due to pressure induced band renormalization. PL peak of GaSe flakes scales linearly with applied vertical pressure, however spiral flakes appear to be more sensitive (dE_{gap}/dP = –1.43 eV GPa^{-1}) to the vertical pressure compared to exfoliated ones (dE_{gap}/dP = –1.17 eV GPa^{-1}) as shown in Figure 5f. For the triangle flake, the slope is similar to that of the spiral flake, but the sample goes to indirect band gap at a lower pressure. The starting point for the triangle is almost the same as the spiral flake, indicating a similar initial in-plane strain. Here, it is worthy to mention that observed difference in the pressure dependence is quite large in comparison to other material systems. For instance, GaN and GaAs belong to the $P6_3mc$ and $F\bar{4}3m$ symmetry groups and dE_{gap}/dP only differ by 0.066 eV GPa^{-1}.[28]

The effect of pressure on the optical band gap of GaSe can be further understood by density functional theory (DFT) calculations. Figure S12 in the Supporting Information shows the band gap of GaSe as a function of vertical pressure obtained by DFT calculations for unstrained (exfoliated) and 2% tensile strained (PVT grown) GaSe layers. Results show that calculated band gap decreases much faster (is more sensitive) for tensile strained GaSe, and agree well with our experimental findings in Figure 5f. Linear fitting of the calculation results gives a

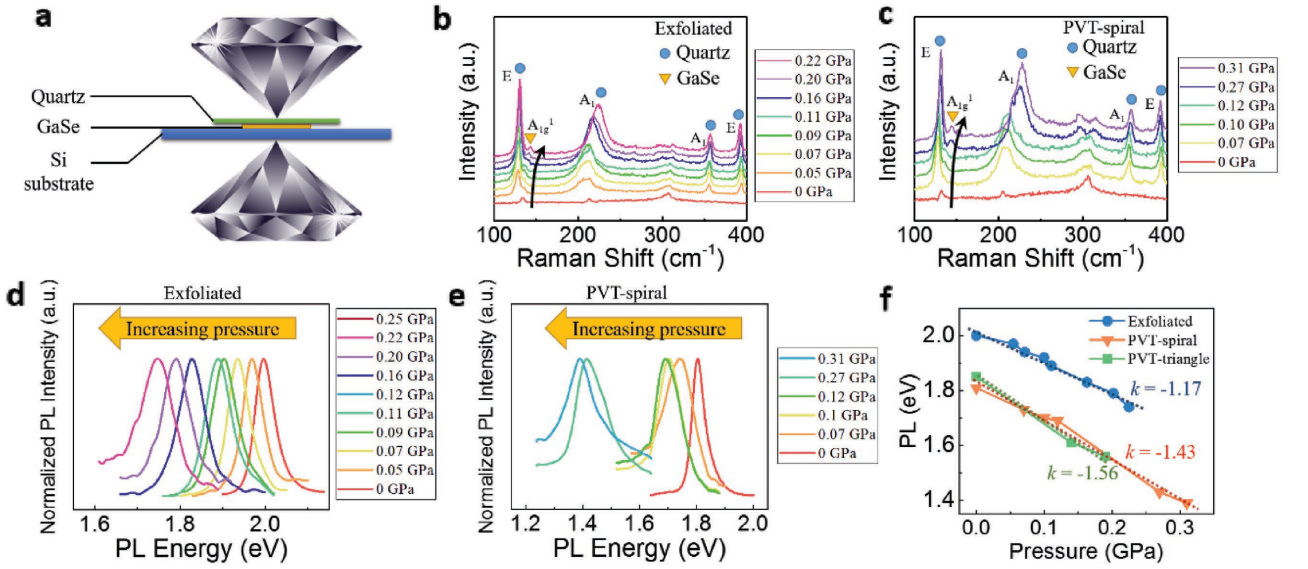

Figure 5. a) Schematic of the experimental setup using a diamond anvil cell. b) Pressure-dependent Raman spectra of exfoliated GaSe. c) Pressure-dependent Raman spectra of PVT synthesized circular flake. d) Pressure-dependent PL spectra of exfoliated GaSe. e) Pressure-dependent PL spectra of PVT synthesized circular flake. f) Band gap as a function of pressure for exfoliated GaSe and PVT synthesized triangle and spiral flakes. Dashed lines are linear fits to each set of data.

Adv. Mater. 2016,
DOI: 10.1002/adma.201601184

dE/dP slope difference of 17%, which is similar to the experimental result of 22%.

Our results mark the very first demonstration of collosal band renormalization effect in GaSe layers grown onto Si(111) surfaces via vdW epitaxy. The band gap spans 620–700 nm range which is significantly red-shifted compared to exfoliated GaSe (620 nm) and covers almost the same spectral range as $GaSe_xTe_{(1-x)}$ ternary alloys. Interestingly, vdW epitaxy on sapphire or GaSe exfoliation onto Si(111) do not yield similar results, suggesting that interaction between Si(111) and GaSe layers play a crucial role especially during nucleation and diffusion of GaSe. Through control over kinetic factors, we were able to synthesize desired GaSe morphologies and attain modest control over emission wavelength. Raman spectroscopy, diamond anvil cell pressure studies, PL spectroscopy, and computational calculations suggest that tensile strain on GaSe layers, arising from interaction between Si and GaSe, results in observed band renormalization effects. Our findings offer new insights in the field of vdW epitaxy and provide a new route for engineering the properties of 2D materials without intentional alloying or applying strain by an external force.

Experimental Section

Sample Preparation: The PVT synthesis of GaSe flakes was carried out in a tube furnace with a 1″ quartz tube. 60 mg GaSe (BOC sciences) and 3 mg Ga_2Se_3 (Alfa Aesar) powders were mixed together as the source materials and Ar was used as the carrier gas. P-type Si (111) wafers were used as growth substrates. Prior to growth the wafers were cleaned with acetone, methanol, RCA-1 cleanser (mixture of DI water, 27% $NH_3{\cdot}H_2O$, and 30% H_2O_2 with volume ratio 5:1:1) and 2% HF. The source powders were loaded in a quartz boat and sent to the center of the tube. The substrate was located 13 cm away downstream. The tube was evacuated to 10 mTorr and then heated from room temperature to 750 °C with a ramping rate of 20 °C min^{-1}. The temperature was kept at 750 °C for 5 min and then cooled down following three paths as shown in Figure 2a and described in the main text. The Ar flow rate was set at 50 sccm and the growth pressure was 30 Torr for the whole process. The growth on sapphire is carried out under the same condition as the triangle growth on Si(111). The sapphire is cleaned by O_2 plasma for 3 min before growth. Exfoliated GaSe, GaSeTe, and GaTe flakes on the same substrates were prepared by mechanical exfoliation from single crystals of each material. The crystals were synthesized by modified Bridgman growth technique[29] in a single zone furnace at temperatures ranging from 850 to 1020 °C for three weeks.

Material Characterization: The morphology and thickness of the GaSe flakes were characterized by a Bruker D3100 Scanning Probe Microscope in ambient environment. The scanning rate was 1 Hz with a resolution of 512 × 512. The data was processed by Gwyddion software. PL and Raman measurements for the as grown samples were performed in a Renishaw InVia spectroscopy system with a 100× objective lens using a laser source with 488 nm wavelength. The laser was focused onto the sample with a spot diameter of 0.5 μm and the power of 0.5 mW. Scanning electron microscopy (SEM) was performed at an accelerating voltage of 3 kV using a Zeiss Gemini Ultra-55 analytical field emission scanning electron microscope equipped with in-lens and secondary electron detectors. Employing a Bruker XFlash 6|60 detector coupled with the SEM, EDS, and element mapping were carried out with an operating voltage of 15 kV for elemental and chemical composition analyses of microscale GaSe flakes. Nano-Auger spectroscopy (n-AES) was performed using an Oxford/Omicron Nano-Auger system that is based on an ultra-high vacuum chamber (base pressure 10^{-10} mbar) equipped with a field emission electron source and a multi-channel hemisphere detector. The electron beam can be focused to a spot size of ≈10 nm enabling the nanoscale chemical composition analysis on microscale GaSe structures. Also, in-depth n-AES studies were conducted employing the Ar ion sputtering gun attached to the instrument. TEM samples were prepared by transferring the flakes from Si to copper grids using PMMA. High-angle annular dark-field imaging was conducted using a NION UltraSTEM100 scanning transmission electron microscope under the acceleration voltage of 60 kV.

High Pressure Measurements: The sample was loaded into a DAC with two diamond located at the top and bottom. A 50 μm thick quartz piece was inserted between the sample and the top diamond to protect the GaSe flakes from being smashed by the diamond. The pressure was tuned by four set screws located symmetrically around the cell. PL and Raman measurements for this experiment was performed in a WITec Alpha 300R Confocal Raman imaging system with a 50× long-working-distance objective lens using a 532 nm laser source. The laser was focused onto the sample with a spot diameter of 1–2 μm and the power of 1.3 mW.

Density Functional Theory Calculations: Our predictions are based on first-principles DFT using projector augmented wave potentials.[30] The exchange correlation potential was represented by the Generalized Gradient characterized by Perdew–Burke–Ernzerhof[31] including vdW[32] correction both for spin-polarized and spin-unpolarized cases. Effects of spin-orbit coupling and non-collinear magnetism were not taken into account. Supercell size, kinetic energy cut-off, and Brillouin zone (BZ) samplings of the calculations were determined after extensive convergence analysis. A plane-wave basis set with kinetic energy cut-off of 370 eV was used. In the self-consistent field potential and total energy calculations BZ was sampled by special k-points. The numbers of these k-points were (16 × 16 × 4) for the primitive bulk ε-GaSe unit cell and were scaled according to the size of the super cells. All atomic positions and lattice constants were optimized by using the conjugate gradient method, where the total energy and atomic forces were minimized. The convergence for energy was chosen as 10^{-6} eV between two consecutive steps, and the maximum Hellmann–Feynman forces acting on each atom was less than 0.01 eV $Å^{-1}$ upon ionic relaxation. The pressure in the unit cell was kept below 5 kBar in each lattice vectors for relax structures. The amplitude of the applied pressure in the calculations conducted under strain was kept under experimentally reachable values.

Supporting Information

Supporting Information is available from the Wiley Online Library or from the author.

Acknowledgements

This work was supported by the Arizona State University seeding program. The authors thank Kedi Wu and Cong Wang for useful discussions. The authors gratefully acknowledge the use of facilities at the LeRoy Eyring Center for Solid State Science at Arizona State University. The authors acknowledge the use of John M. Cowley Center for High Resolution Electron Microscopy at Arizona State University. SEM and EDS experiments at the Molecular Foundry were supported by the Office of Science, Office of Basic Energy Sciences, of the U.S. Department of Energy under Contract No. DE-AC02-05CH11231. S.T. acknowledges funding from NSF DMR-1552220 and CMMI-1561839.

Received: February 29, 2016
Revised: April 13, 2016
Published online:

[1] W. Huang, L. Gan, H. Li, Y. Ma, T. Zhai, *CrystEngComm*. **2016**, DOI:10.1039/C5CE01986A.
[2] V. Zólyomi, N. D. Drummond, V. I. Fal'ko, *Phys. Rev. B* **2013**, *87*, 195403.

[3] S. Lei, L. Ge, Z. Liu, S. Najmaei, G. Shi, G. You, J. Lou, R. Vajtai, P. M. Ajayan, *Nano Lett.* **2013**, *13*, 2777.
[4] D. J. Late, B. Liu, J. Luo, A. Yan, H. S. S. R. Matte, M. Grayson, C. N. R. Rao, V. P. Dravid, *Adv. Mater.* **2012**, *24*, 3549.
[5] a) P. Hu, Z. Wen, L. Wang, P. Tan, K. Xiao, *ACS Nano* **2012**, *6*, 5988; b) P. Hu, L. Wang, M. Yoon, J. Zhang, W. Feng, X. Wang, Z. Wen, J. C. Idrobo, Y. Miyamoto, D. B. Geohegan, K. Xiao, *Nano Lett.* **2013**, *13*, 1649; c) F. Liu, H. Shimotani, H. Shang, T. Kanagasekaran, V. Zólyomi, N. Drummond, V. I. Fal'ko, K. Tanigaki, *ACS Nano* **2014**, *8*, 752.
[6] X. Li, M.-W. Lin, A. A. Puretzky, J. C. Idrobo, C. Ma, M. Chi, M. Yoon, C. M. Rouleau, I. I. Kravchenko, D. B. Geohegan, *Scientific Rep.* **2014**, *4*, 5497.
[7] Y. Zhou, Y. Nie, Y. Liu, K. Yan, J. Hong, C. Jin, Y. Zhou, J. Yin, Z. Liu, H. Peng, *ACS Nano* **2014**, *8*, 1485.
[8] H. L. Zhuang, R. G. Hennig, *Chem. Mater.* **2013**, *25*, 3232.
[9] a) K. Saiki, K. Ueno, T. Shimada, A. Koma, *J. Cryst. Growth* **1989**, *95*, 603; b) A. Koma, *Thin Solid Films* **1992**, *216*, 72.
[10] F. Ohuchi, B. Parkinson, K. Ueno, A. Koma, *J. Appl. Phys.* **1990**, *68*, 2168.
[11] T. Tsirlina, S. Cohen, H. Cohen, L. Sapir, M. Peisach, R. Tenne, A. Matthaeus, S. Tiefenbacher, W. Jaegermann, E. Ponomarev, *Solar Energy Mater. Solar Cells* **1996**, *44*, 457.
[12] R. Schlaf, N. Armstrong, B. Parkinson, C. Pettenkofer, W. Jaegermann, *Surf. Sci.* **1997**, *385*, 1.
[13] L. Zhou, K. Xu, A. Zubair, A. D. Liao, W. Fang, F. Ouyang, Y.-H. Lee, K. Ueno, R. Saito, T. Palacios, *J. Am. Chem. Soc.* **2015**, *137*, 11892.
[14] A. Klein, O. Lang, R. Schlaf, C. Pettenkofer, W. Jaegermann, *Phys. Rev. Lett.* **1998**, *80*, 361.
[15] a) Y. Gong, J. Lin, X. Wang, G. Shi, S. Lei, Z. Lin, X. Zou, G. Ye, R. Vajtai, B. I. Yakobson, *Nat. Mater.* **2014**, *13*, 1135; b) Y. Zhan, Z. Liu, S. Najmaei, P. M. Ajayan, J. Lou, *Small* **2012**, *8*, 966; c) Y. Shi, W. Zhou, A.-Y. Lu, W. Fang, Y.-H. Lee, A. L. Hsu, S. M. Kim, K. K. Kim, H. Y. Yang, L.-J. Li, *Nano Lett.* **2012**, *12*, 2784; d) S. Najmaei, Z. Liu, W. Zhou, X. Zou, G. Shi, S. Lei, B. I. Yakobson, J.-C. Idrobo, P. M. Ajayan, J. Lou, *Nat. Mater.* **2013**, *12*, 754.
[16] S. Liu, X. Yuan, P. Wang, Z.-G. Chen, L. Tang, E. Zhang, C. Zhang, Y. Liu, W. Wang, C. Liu, *ACS Nano* **2015**, *9*, 8592.
[17] a) C. P. Kuo, S. K. Vong, R. M. Cohen, G. B. Stringfellow, *J. Appl. Phys.* **1985**, *57*, 5428; b) Y. Ishikawa, K. Wada, D. D. Cannon, J. Liu, H.-C. Luan, L. C. Kimerling, *Appl. Phys. Lett.* **2003**, *82*, 2044; c) R. Chen, H. Lin, Y. Huo, C. Hitzman, T. I. Kamins, J. S. Harris, *Appl. Phys. Lett.* **2011**, *99*, 181125; d) W. Zhou, Y. Liu, Y. Yang, P. Wu, *J. Phys. Chem. C* **2014**, *118*, 6448.
[18] a) M. Eddrief, C. Sébenne, A. Sacuto, M. Balkanski, *J Cryst. Growth* **1994**, *135*, 1; b) Y. Zheng, A. Koëbel, J. Pétroff, J. Boulliard, B. Capelle, M. Eddrief, *J. Cryst. Growth* **1996**, *162*, 135; c) R. Rudolph, C. Pettenkofer, A. A. Bostwick, J. A. Adams, F. Ohuchi, M. A. Olmstead, B. Jaeckel, A. Klein, W. Jaegermann, *New J. Phys.* **2005**, *7*, 108.
[19] E. Bauer, J. H. van der Merwe, *Phys. Rev. B* **1986**, *33*, 3657.
[20] a) S. A. Morin, A. Forticaux, M. J. Bierman, S. Jin, *Nano Lett.* **2011**, *11*, 4449; b) A. Zhuang, J. J. Li, Y. C. Wang, X. Wen, Y. Lin, B. Xiang, X. Wang, J. Zeng, *Angew. Chem. Int. Ed.* **2014**, *53*, 6425.
[21] W. K. Burton, N. Cabrera, F. C. Frank, *Phil. Trans. R. Soc. Lond. A: Math. Phys. Eng. Sci.* **1951**, *243*, 299.
[22] D. Rybkovskiy, N. Arutyunyan, A. Orekhov, I. Gromchenko, I. Vorobiev, A. Osadchy, E. Y. Salaev, T. Baykara, K. Allakhverdiev, E. Obraztsova, *Phys. Rev. B* **2011**, *84*, 085314.
[23] a) P. Lu, X. Wu, W. Guo, X. C. Zeng, *Phys. Chem. Chem. Phys.* **2012**, *14*, 13035; b) C. Zhu, G. Wang, B. Liu, X. Marie, X. Qiao, X. Zhang, X. Wu, H. Fan, P. Tan, T. Amand, *Phys. Rev. B* **2013**, *88*, 121301.
[24] H. J. Conley, B. Wang, J. I. Ziegler, R. F. Haglund Jr., S. T. Pantelides, K. I. Bolotin, *Nano Lett.* **2013**, *13*, 3626.
[25] T. Mohiuddin, A. Lombardo, R. Nair, A. Bonetti, G. Savini, R. Jalil, N. Bonini, D. Basko, C. Galiotis, N. Marzari, *Phys. Rev. B* **2009**, *79*, 205433.
[26] A. Castellanos-Gomez, R. Roldán, E. Cappelluti, M. Buscema, F. Guinea, H. S. van der Zant, G. A. Steele, *Nano Lett.* **2013**, *13*, 5361.
[27] K. Zhang, S. Hu, Y. Zhang, T. Zhang, X. Zhou, Y. Sun, T.-X. Li, H. J. Fan, G. Shen, X. Chen, N. Dai, *ACS Nano* **2015**, *9*, 2704.
[28] a) G. Franssen, T. Suski, A. Kamińska, J. P. Viterbo, E. M. Merino, E. Lliopoulus, A. Georgakilas, S. Che, Y. Ishitani, A. Yoshikawa, *J. Appl. Phys.* **2008**, *103*, 033514; b) B. Welber, M. Cardona, C. Kim, S. Rodriguez, *Physical Review B* **1975**, *12*, 5729; c) W. Shan, J. Ager III, K. Yu, W. Walukiewicz, E. Haller, M. Martin, W. McKinney, W. Yang, *J. Appl. Phys* **1999**, *85*, 8505.
[29] Y. Ni, H. Wu, C. Huang, M. Mao, Z. Wang, X. Cheng, *J. Cryst. Growth* **2013**, *381*, 10.
[30] P. E. Blöchl, *Phys. Rev. B* **1994**, *50*, 17953.
[31] J. P. Perdew, K. Burke, M. Ernzerhof, *Phys. Rev. Lett.* **1996**, *77*, 3865.
[32] S. Grimme, *J. Comput. Chem.* **2006**, *27*, 1787.

Adv. Mater. **2016**,
DOI: 10.1002/adma.201601184